JOURNAL OF X-RAY SCIENCE AND TECHNOLOGY **5**, 207–220 (1995)

# Performance Model for High Spatial Resolution CsI Scintillator Screens Coupled to CCD Detectors

CHRISTIAN M. CASTELLI[1] AND NIGEL M. ALLINSON[2]

*Department of Electronics, University of York, Heslington, York, YO1 5DD, United Kingdom*

Received July 5, 1994; revised November 21, 1994

A performance model for an x-ray imaging camera that is currently being developed at York University for the recording of crystallographic diffraction patterns produced by synchrotron radiation is presented. The camera is based on charge coupled device (CCD) sensors which are coupled to a CsI(Tl) x-ray scintillator screen using 3:1 reducing fiber optic tapers. The model predicts the accuracy to which diffraction spot intensities can be measured over a range of incident x-ray flux. The effect of the point spread function of the scintillator and optics and the typical expected diffraction spot geometry is included in the model and shown to have the most significant effect on the system performance for low spot intensities, limiting the camera's effective dynamic range. However, it is shown that quantum limited performance for incident dose fluxes as low as 100 photons per spot can be readily achieved in this design. Finally, the camera performance is predicted for x-ray energies above the scintillator *K* absorption edges (>33 keV). The effects of energy loss through scintillation *K* shell fluorescent escape photons reduces the camera's detective quantum efficiency. 

## 1. INTRODUCTION

In recent years there has been intensive work in the area of x-ray instrumentation for the recording of crystallographic diffraction patterns produced by synchrotron radiation sources. However, this application places great demands on detector performance. Large, sensitive imaging areas, at least 150 × 150 mm, are necessary to record the full diffraction pattern. The detector needs to be able to cope with high global count rate (typically $5 \times 10^6$ photons/s at a wiggler beam-line on a second generation synchrotron source), together with a local count rate of greater than $10^4$ photons/s for each diffraction spot. Other important parameters include complete images at least every 5 s, as a complete data set may consist of several hundred images as the crystal is rotated, and a dynamic range greater than $10^3$ to record both weak and intense diffraction spots with a high degree of accuracy.

Several groups are currently developing large-aperture cameras based on x-ray scintillators coupled to CCD detectors using fiber optic tapers (*3, 4*). These novel instruments promise a large imaging area with high detection efficiency and rapid throughput compared to conventional detectors.

[1] Current address: Department of Physics and Astronomy, University of Leicester, University Road, Leicester LE1 7RH, United Kingdom. E-mail address: cmc@star.le.ac.uk.

[2] E-mail address: nma@ohm.york.ac.uk.



0895-3996/95 $6.00

Currently, routine x-ray crystallographic data are collected at an energy of around 8 keV (1.5 Å). However, there is strong evidence that higher energies increase the radiation tolerance of the samples, particularly protein structures (*1*). For this reason, data collection at 14 keV (0.9 Å) using bending magnets and wigglers is not uncommon. Furthermore, the potential use of ultra-short wavelength energies from undulator harmonics around 37 keV (0.33 Å) and the advent of third-generation synchrotron sources such as the European Synchrotron Radiation Facility (ESRF) suggest that there is a need for detectors with sensitivity up to 40 keV (*2*).

This paper will present a theoretical model that is used to predict the performance of a large-aperture detector system that is currently being developed at York University. In this model, the detective quantum efficiency (DQE) is used to determine the accuracy to which the spot dose (total number of incident x-ray photons per image spot) can be measured. Typically, the DQE is modeled for single x-ray events where all of the signal is assumed to be confined to a single detector pixel. It is apparent that the DQE models based on this assumption do not necessarily give a realistic estimate of the camera performance since the finite diffraction spot size will require the summation of charge from several noisy image pixels. More importantly, however, is the effect of signal lost from the peripheral pixels in the diffraction spot due to the finite instrument point spread function (PSF). This is particularly important for low-dose measurements and it will be shown that a significant loss of detector performance from that predicted for the simple single-event model will occur, resulting in a more limited useful detector dynamic range. The model will use actual values for the PSF of the scintillator and optics of a taper/CCD camera system currently under development. Finally, for x-ray energies greater than the scintillator *K* absorption edges (>33 keV), the effects of *K* shell fluorescence on the camera DQE are rarely considered. It will be shown that the DQE for x rays of incident energy above the *K* edge is significantly reduced from the values predicted using a simple model based solely on the absorption of the scintillator.

## 2. INSTRUMENT CONCEPT

The CCD detector is the pre-eminent electro-optic detector for imaging in the UV/optical and soft x-ray wavelengths. It offers good quantum efficiency in the visible/UV and because of its excellent linearity and very low noise levels (as low as 3 electrons rms) has excellent spectroscopic performance at soft x-ray wavelengths (*5*). Although the CCD can also be used to directly detect the x rays with good efficiency up to 10 keV through the use of high resistivity substrates (*6*), the high internal gain severely limits the dynamic range of the device. For silicon ~3.7 eV of photon energy is required to create an electron hole pair (*7*). Thus for an 8 keV photon 2,200 signal electrons will be created per x-ray interaction, giving a dynamic range of ~100 for typical charge handling capacity of CCDs. In this case, dynamic range is defined as the ratio of the maximum signal handling capacity of the CCD to the noise floor. Furthermore, CCD imaging areas are currently limited to a maximum of 5 × 5 cm which is insufficient to acquire all of the diffraction pattern. However, excellent spatial resolution is possible and direct detection has found application in time resolved studies where a small area of the CCD is rapidly read out (*8*).

A promising way of satisfying both the requirements for a large area and high dynamic range is to use a scintillator as the primary converter and fiber optic tapers

TABLE 1

Measured Transmission Values for Lenses and Tapers Taken from Ref. (*9*)

| De-magnification | Lens | Taper | Ideal |
|---|---|---|---|
| 1:1 | 12% | 80% | 100% |
| 2:1 | 5% | 20% | 25% |
| 10:1 | 0.1% | 0.75% | 1% |

to reduce the image to the format of the CCD. The use of a taper is essential in the design as their high numeric aperture means the transmission efficiency is significantly higher than a lens for a given demagnification ratio when viewing a Lambertian source. Custom lens design can yield lenses with high numeric aperture at a specific wavelength, but suffer from light scatter at the surfaces and are also extremely expensive. Table 1 shows measured transmission values for different demagnification ratios of tapers and lenses (*9*). Large imaging areas can then be built out of a mosaic of camera modules as shown in Fig. 1. However, for a high DQE, there is a limit to the transmission loss that can be suffered. For practical purposes a demagnification of $\sim$3:1 is considered to be the limit for most x-ray scintillators since higher ratios will further reduce the transmission so that the overall camera gain (signal electrons per interacting x ray) is poorly matched to the CCD detector noise level (10 to 40 electrons rms).

The scintillator chosen for our camera design is CsI(Tl) as this scintillator has many characteristics that make it suitable for x-ray imaging applications. It can be easily evaporated onto glass substrates, has the high density (4.5 g/cm$^3$) necessary for good x-ray detection efficiency (up to 30 keV), is nonhygroscopic, and has no measurable long-lived scintillation components above the 0.01% level (*10*). The scintillation effi-

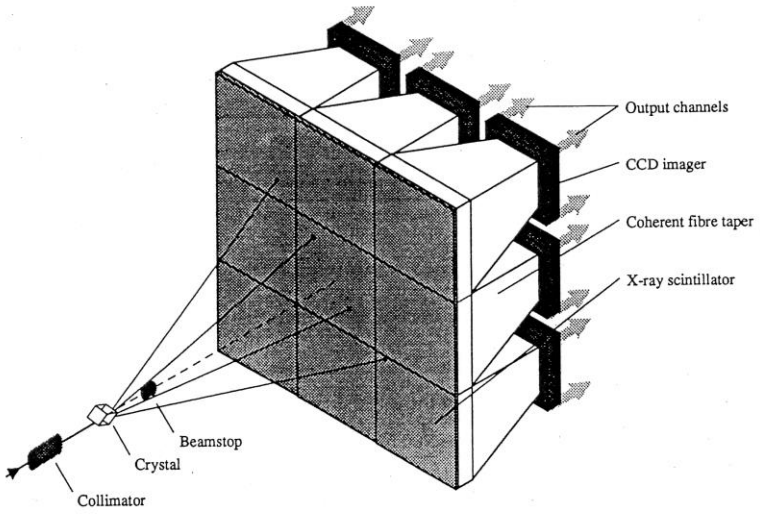


FIGURE 1

ciency for CsI(Tl) is around 11%, and this yields a CCD signal of 30 electrons per x-ray photon (assuming typical values for the instrument concept) at 8 keV and is therefore well matched to the noise levels of the CCD. For the highest x-ray absorption at 8 keV, a relatively thick scintillator layer of thickness $\sim 100\ \mu$m is required. However, the spatial resolution of scintillators is significantly degraded by the diffusion of light as it travels from the x-ray interaction point to the fiber optic surface. Even though evaporated CsI is observed to display a vertical, needle-like growth structure that improves the spatial resolution by channeling of the light (*11*), the scintillator PSF still exhibits an extended profile over diameters several times the scintillator thickness.

To preserve the spatial resolution the scintillator for our camera system comprised an array of isolated CsI columns. Light emitted within the critical angle for CsI then reflects down the column towards the fiber optic taper with minimal lateral diffusion. The fraction of light trapped in the column is derived from the solid angle subtended by the light cone at the critical angle, assuming a reflectively coated surface layer. This can be estimated from the values of the refractive index, which for CsI is 1.8 at the peak scintillation light output wavelength of 550 nm. This gives a value of approximately 83% for the fraction of light that is piped to the fiber optics (*12*). Scattered light outside the critical angle is absorbed by the presence of ema cladding in the fiber optic taper. The fraction of light transmitted and the fill factor for the fibre optic taper ($\sim$80%) are taken into account when calculating the scintillator efficiency for the performance model.

It has been demonstrated that under the appropriate conditions, evaporated CsI will grow in such a way that the structure of the underlying substrate is mirrored in the final scintillator layer (*13*). Thus, to produce a structured scintillator layer on the fiber optic taper, the surface was prepared following the technique described in (*14*). In this technique, the face plate was selectively etched to remove the cladding glass from around each fiber optic core, thus producing a surface composed of many discrete glass columns. By evaporation onto this surface, the scintillator was found to grow as an extension of the core glass columns, resulting in a segmented scintillator screen. To illustrate the improvement in spatial resolution, Fig. 2 shows the PSF expressed in terms of the integrated charge within a given radius for both a structured/segmented scintillator and a uniform scintillator layer which was deposited onto a flat fiber optic surface. The layer thicknesses were both 30 $\mu$m and it can be seen that the scintillator produced on the etched taper has a much improved PSF, with 70% of the charge contained within a 3-pixel radius compared to 12 pixels for the uniform layer. The performance of this scintillator screen is explained in greater detail in (*15*). It should be noted that the resolution quantified in this manner is a more meaningful measurement than the more commonly used FWHM which can give an acceptable value for the PSF but yields little information about the total signal collected within the central pixels in the presence of the extended distribution of the PSF. The PSF measured for the segmented screen is used in the performance model of the camera system.

## 3. DETECTOR DQE AND RELATIVE DOSE UNCERTAINTY

The fundamental parameter for assessing the performance of the x-ray camera is the detective quantum efficiency (*16*). It relates the detection efficiency of an ideal

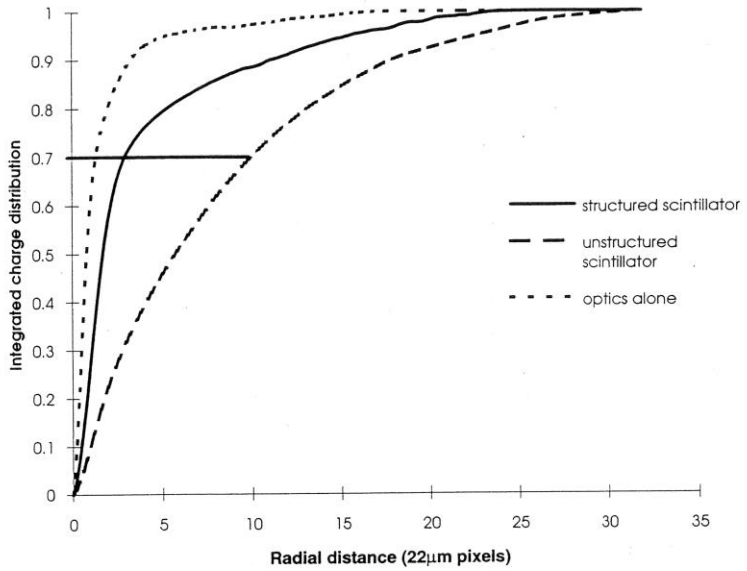


FIGURE 2

detector to an actual detector in terms of the precision to which a measurement can be made. The definition of DQE is given by

$$\mathrm{DQE} = \frac{(S_0/\sigma_0)^2}{(S_i/\sigma_i)^2}, \qquad [1]$$

where S is the signal, $\sigma$ is the noise, and the subscripts i and o refer to the input and output signal and noise respectively. In an ideal detector the DQE is unity, but the addition of noise at any stage in the signal chain and/or the loss of signal will reduce the DQE. After (*17*), the relative system variance, $R_{\mathrm{total}}$, can be expressed as the sum of all the relative variances of each stage in the detection chain. This can be expressed as

$$R_{\mathrm{total}} = \left(\frac{\sigma_0}{S_0}\right)^2 = R_0 + \frac{R_{\mathrm{s}}}{\epsilon N_0} + \frac{R_{\mathrm{opt}}}{\epsilon N_0 g_s} + \frac{R_{\mathrm{ccd}}}{\epsilon N_0 g_s T_f} + R_\eta, \qquad [2]$$

where $R_0$ is the Poisson variance of the x-ray source flux, $R_{\mathrm{s}}$ is the variance ion the number of scintillation output light photons, $R_{\mathrm{opt}}$ is the variance from image to image introduced by the finite transmission of the taper, $R_{\mathrm{ccd}}$ is the variance arising from the finite detection efficiency of the CCD, $R_\eta$ is the additional variance imposed on the recorded image by the detector noise, $g_{\mathrm{s}}$ is the number of scintillation photons per interacting x ray that reach the scintillator/optics interface, $N_0$ is the incident number of x-ray photons, $\epsilon$ is the scintillator absorption, and $T_{\mathrm{f}}$ is the transmission of the fiber

optic taper. The relative variances of each stage of the detection process are tabulated in Table 2 where $\eta_{ccd}$ is the CCD quantum efficiency and $R_\eta$ is expressed in terms of the equivalent noise, $n_{eff}$, which is the ratio of the CCD rms noise to the signal produced for a single x-ray photon incident on the scintillator. Substituting the terms in Table 2 into Eq. [2] and expanding and simplifying the expression, then

$$R_{total} = \frac{1}{\epsilon N_0}\left[1 + \frac{1}{g_s T_f \eta_{ccd}}\right] + R_\eta. \quad [3]$$

In Eq. [3], the term $g_s T_f \eta_{ccd}$ is just the number of electron–hole pairs produced in the CCD per interacting photon. The steps from the absorption of the x ray to the creation of the electron–hole pair can now be viewed as one complex step. Thus, the contributions to the variance need only be assessed at statistical, local quantum minima where the product of the term is much less than unity. The expression for the total relative variance can now be used to determine the detective quantum efficiency of the whole instrument through the following relationship:

$$\mathrm{DQE} = \frac{1}{R_{total} N_0}. \quad [4]$$

When considering the camera performance, it is often more intuitive to determine the relative dose uncertainty, $\rho$, which is the precision to which a dose measurement in a single CCD pixel can be made. This parameter in turn is simply related to the DQE by

$$\rho = 1/\sqrt{\mathrm{DQE} \times N_0} = \sqrt{R_{total}}. \quad [5]$$

This expression will be used to predict the camera performance in the next section, using appropriate parameters for the transmission and detection stages of the camera.

## 4. TYPICAL SYSTEM PERFORMANCE

The relative dose uncertainty, as defined by Eq. [4], can now be predicted for a typical system as a function of signal level. For the CCD detector, a scientific slow-

TABLE 2

Relative Variances for Each Gain and Detection Process of the X-Ray Camera

| Statistical process | Process variance | Distribution type |
|---|---|---|
| Absorption of x-ray photons by scintillator (Ro) | $1/\epsilon N_0$ | Poisson |
| Scintillator light output Rs | $1/g_s$ | Poisson |
| Transmission of scintillator photons (Ropt) | $1/T_f^{-1}$ | Binomial |
| Detection of scintillator photons by CCD (Rccd) | $1/\eta_{ccd}^{-1}$ | Binomial |
| Addition of camera noise ($R\eta$) | $n_{eff}^2/N_0^2$ | Poisson |

scan operating mode is usually employed for low-noise detector operation. The buildup of dark current during CCD image integration periods can be suppressed by cooling the device. An operating temperature of around −60°C will give a dark current generation rate of ~0.1 electrons per pixel per second, thus giving a negligible dark charge signal in the array for periods of several seconds. The CCD and electronics noise value assumed for the model is around 40 electrons rms and is typical of camera systems employing correlated double sampling techniques to remove CCD reset noise at a pixel readout rate of 500 kHz.

The scintillator light output has been measured for various structured scintillator screens and a figure of around 400 photons per x-ray interaction is typical and compares well with other measured values of the scintillation conversion efficiency of 11% (*18*). The scintillator light emission from CsI(Tl) peaks at around 550 nm and extends from 400 to 700 nm. In this band the highest CCD quantum efficiency is achieved through back-illuminated technology. Sensors of this type are available in conjunction with antireflection coatings to give around 70% peak detection efficiency in this band. Using the quantum efficiency curves for CCD sensors produced by EEV Ltd., the integrated efficiency of the CCD is around 57%. The scintillation thickness is 100 $\mu$m in this example and will absorb essentially 100% of the x-ray flux at 8 keV. Finally, the combined transmission of a 2.5:1 optical taper and face-plate coupler used in the model is around 11%, calculated from the manufactures measurements.

Figure 3 shows the relative dose uncertainty as a function of incident photon flux. The ideal curve is the predicted performance for an ideal detector possessing negligible noise and no system losses and is given by $1/\sqrt{N_0}$. At high dose levels, the camera curve tends toward the ideal performance, showing that in this range of flux levels the camera is solely limited by the statistics of the x-ray source. The camera performance is then said to be quantum limited. These curves therefore show that the CCD/taper camera can have near ideal performance for an incident flux of only a few x-ray

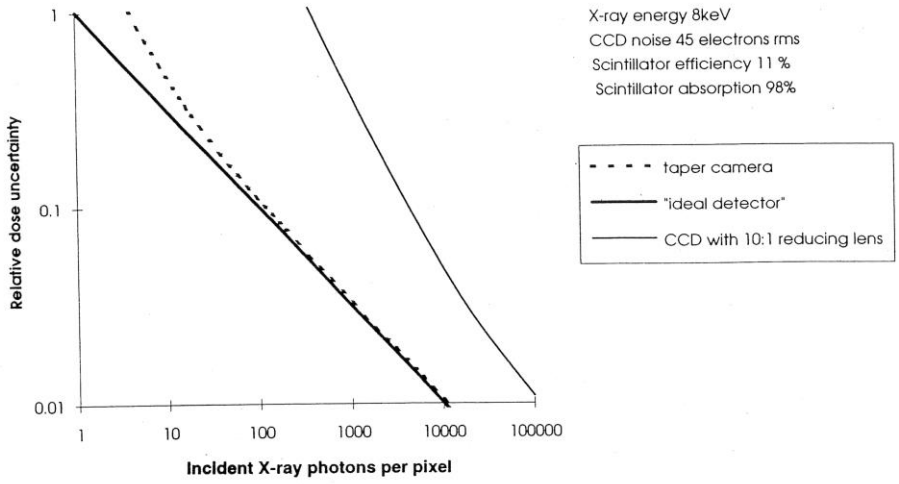


FIGURE 3

photons. For comparison, the camera performance for a lens-based system possessing the same input aperture as the taper mosaic employing a 10:1 demagnifying lens is shown. This curve shows a sharp departure from quantum limited performance at a much higher incident dose than the CCD/taper system and is due to the reduced signal to noise ratio for the final CCD detection stage of the camera caused by the less efficient lens transmission.

### *4.1. Effect of Scintillator Resolution and Diffraction Spot Size for Low Contrast Imaging*

For protein crystallography the size of the Bragg spots is determined by the input beam collimation which is usually set to give 300 $\mu$m diameter diffraction spots (see Fig. 1). The diffraction spot therefore extends over many CCD pixels and so the final term in Eq. [5] describing the effect of the CCD noise on the DQE has to be modified to account for the summation of several "noisy" image pixels. Furthermore, at low incident x-ray doses, where the x-ray-generated signal in a given image pixel is comparable to the CCD noise level, there will be a reduction in the dose measurement accuracy. This arises because of the requirement to threshold the image pixels to reject noise events from those generated by an x-ray event. Typically, a $5\sigma$ threshold is employed ($\sigma^2$ is the CCD noise variance) to reject 99.99% of noise events. Also, in a real imaging application, there is the x-ray background which will add further noise to the final recorded image. This will be very dependent on the crystal sample, diffraction spot intensity, and geometry of the system and so for simplicity has not been considered by this performance model. The model must therefore be extended to address signals over multiple pixels to predict the dose accuracy.

To determine the effects of these factors on camera performance, a Monte-Carlo method was employed to simulate the detection of signal photons in the CCD array. X-ray interaction events were randomly distributed in the diffraction spot area given by the collimator diameter. The point-spread function of the scintillator and optics was then used to blur the scintillator photons into an extended profile which is the convolution of the collimator profile with the instrument PSF. The demagnification of the taper was taken into account to scale the final image spot. Other distortions or non-uniformities, which may be present in the fiber optic taper or in the fiber optic-to-CCD bonding, were not addressed. A CCD pixel binning size of $2 \times 2$ pixels was chosen to provide adequate sampling of the image whilst minimizing the effects of the CCD pixel noise. The integrated intensity of many simulated diffraction spots was obtained at various incident x-ray doses with the criterion used to reject random noise "events" from the CCD being that the x-ray generated signal in a given pixel must be greater than $5\sigma$, where $\sigma$ is the rms CCD noise. The statistical variance in the integrated intensity values for the simulated spots was then used to calculate the dose uncertainty which is shown in Fig. 4. The figure shows the predicted response for a binned detection of 300 $\mu$m diameter-diffused spot (open circles) to a single event in a single-pixel mode (solid line). At low x-ray fluxes, the camera performance for diffuse-spot imaging rapidly deviates from the single pixel mode approximation, showing a dramatic reduction in the ability of the camera to perform quantitative x-ray analysis below an incident dose level of $\sim$100 x-ray photons/frame. However, reasonable counting sta-

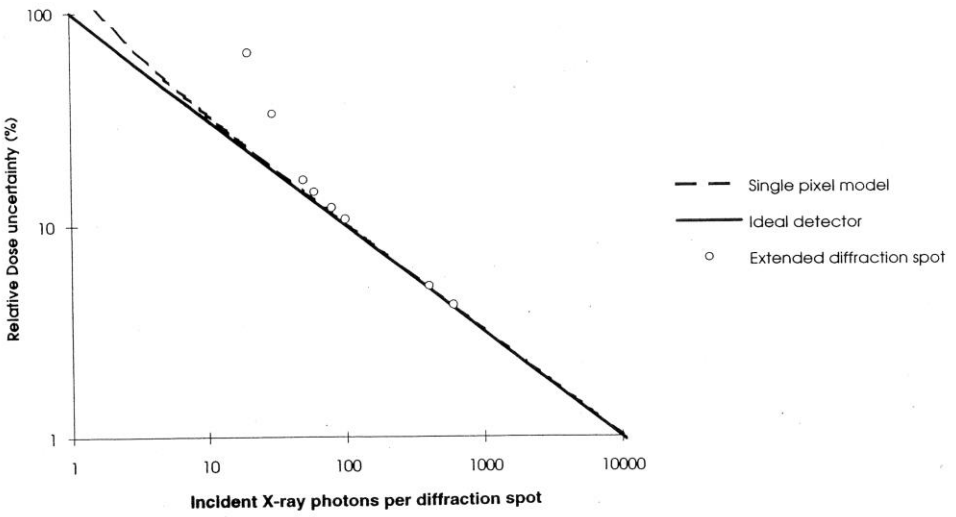


FIGURE 4

tistics can still be obtained for incident flux levels down to this level, but this performance will be dramatically reduced further if a uniform scintillator is used which does not preserve the spatial resolution.

Finally, it should be noted that there will be a tradeoff between taper ratio and DQE since higher ratios will reduce the image scale, thereby relaxing the requirements on the scintillator resolution. However, at some point the reduction in the overall system gain will effect the signal-to-noise ratio of the camera. For the camera system proposed the optimal taper ratio is around 3 and for camera systems with poorer spatial resolution this optimal value will be much higher.

## 5. EFFECTS OF SCINTILLATOR ABSORPTION EDGES

In a scintillator, the energy deposited by each x-ray interaction will not be a constant and will be distributed according to some energy distribution function. This may arise from light scatter in the optics and the loss of x-ray energy by the escape of $K$ fluorescence photons. In a thick, 100-$\mu$m CsI scintillator, the $K$ escape fraction can be as high as 50%, resulting in a range of pulse-height distributions for a single input energy. In this case the simple signal-to-noise relationship needs to be modified to account for this signal loss and additional noise variance introduced by the energy pulse height distribution function. Swank (*19*) has derived an expression that relates the signal-to-noise ratio for a broad pulse-height spectrum to that of a line spectrum by modifying the absorption parameter with a second parameter termed the scintillation efficiency $A_s$. In this case, the signal-to-noise ratio for the energy deposited in the scintillator is expressed as

$$\text{signal:noise} = \sqrt{N_0 \epsilon A_s}, \qquad [6]$$

where the parameter $A_s$ is defined as

$$A_s = \frac{M_1^2}{M_2 M_0} \quad [7]$$

and $M_k$ is the $k$th moment of the pulse height distribution. This is given by

$$M_k = \sum_i n(E)_i E_i^k, \quad [8]$$

where $n(E)$ is the occurrence of the scintillation pulse height $E$ in the broad spectrum. Including the term describing the effect of the broad scintillation spectrum in Eq. [4], the total relative variance of the camera becomes

$$R_{\text{total}} = \frac{1}{\epsilon N_0}\left[1 + \left(\frac{1}{A_s} - 1\right) + \frac{1}{g_s T_f \eta_{\text{ccd}}}\right] + R_\eta \quad [9]$$

Since the produce of the high scintillator light yield, taper transmission, and CCD quantum efficiency is $\gg 1$, this term can be neglected. Substituting Eq. [9] into [4] and simplifying, the DQE is given by

$$\text{DQE} = \frac{\epsilon A_s N_0}{N_0 + \epsilon A_s n_{\text{eff}}^2}. \quad [10]$$

This expression is similar to that derived in (*16*) except that the absorbed fraction is modified by the term $A_s$. For incident x-ray energies above the $K$ edges of the scintillator, $A_s$ has a value of less than unity and the DQE of the detector will therefore be reduced. In order to predict the value of $A_s$ over the range of x-ray energies, a Monte-Carlo method was employed to simulate x-ray interaction in CsI and to obtain estimates of the scintillator parameters.

### *5.1. Calculation of the Scintillator Parameters*

To calculate the effects of energy loss within the scintillator that arise from $K$-shell fluorescence, details of the x-ray interaction in CsI are required. This section describes the interaction and presents results of a Monte-Carlo simulation used to determine the scintillator parameters as a function of x-ray energy and scintillator thickness.

*5.1.1. Description of the x-ray interaction in CsI.* The x-ray interaction in CsI is complex, consisting of a cascade of fluorescent photons and low energy photoelectrons. Above the $K$ edges in CsI, the most probable interaction is with the atomic $K$ shells and, because of the high fluorescent yield, atomic de-excitation is predominantly through the emission of a characteristic $K$ fluorescent photon. The absorption length of the fluorescent photon is large, ~200–250 $\mu$m, and so the probability that it will escape from a scintillator layer without further interaction is high. This will therefore result in a significant fraction of the incident x-ray energy being lost and a reduction in the performance of the screen. Also, a further interaction is possible when the

cesium $K$ fluorescent photon interacts with an iodine atom. In this case, the iodine atom may emit a $K$ fluorescent photon resulting in a photon cascade, leading to a high escape probability for the cesium $K$ shell interactions in the scintillator. Finally, for the $L$ shell interactions the $L$ fluorescent yield is much lower ($\sim$10%) and, coupled with the low x-ray energy of the fluorescent photon ($\sim$4 keV), the effects of these interactions on the scintillator performance are small.

The parameters used to determine the probabilities of the various interactions are shown in Table 3. The probability of a particular interaction occurring can be calculated from the product of all individual probabilities. To illustrate this, the probability of an x-ray interaction giving rise to a cesium $K\alpha$ fluorescent photon is given by the product of the interaction probability for the cesium atom, the interaction probability for the $K$ shell, the $K$ shell fluorescent yield, and finally the $K\alpha$ fluorescence probability ($0.54 \times 0.824 \times 0.945 \times 0.813 \sim 34\%$). Consistent values for these parameters can be found in (*20, 21*) and, to simplify the simulation, an empirical set of equations was used to determine the absorption coefficients for cesium and iodine within the energy range of interest. These empirical equations along with parameters used to fit the curves to the experimentally determined absorption coefficients are given in Ref. (*22*).

*5.1.2. Monte-Carlo simulation of the x-ray interaction.* The simulation uses a logarithmic method for generating random, exponentially distributed absorption depths which are weighted according to the attenuation coefficients for CsI. For each x-ray interaction the probabilities given in Table 3 are used to determine the x-ray de-excitation path. For the $K$ shell fluorescent photons, they are assumed to be emitted isotropically and for each fluorescent photon a random absorption length is then generated for the emission line energy. This is then used to determine the next interaction point in the scintillator and if this is outside the layer the photon event is classed as an escape event. If the photon is reabsorbed then the process repeats until the photon is wholly absorbed or lost. The final energy deposited in the scintillator for each initial x-ray interaction is recorded.

TABLE 3

X-Ray Interaction Parameters

| Scintillator element: | Iodine | Caesium |
|---|---|---|
| Absorption edge (keV) | 33.2 | 35.96 |
| $K\alpha$, $\beta$ photon energy (keV) | 28.5, 32.5 | 30.8, 35.5 |
| $L$ photon energy (keV) | 4.0 | 4.3 |
| $K$ photon absorption length ($\mu$m) | $\sim$200 | $\sim$260 |
| Interaction probability for atom | 0.46 | 0.54 |
| $K$ shell interaction probability (Energy > $K$ edge) | 0.826 | 0.824 |
| $L$ shell interaction probability (Energy < $K$ edge) | 1.0 | 1.0 |
| $K$ shell fluorescent yield | 0.935 | 0.945 |
| $K\alpha$ emission probability | 0.813 | 0.813 |
| $K\beta$ emission probability | 0.187 | 0.187 |
| $L$ shell fluorescent yield | 0.103 | 0.118 |

*5.1.3. The scintillator parameters.* The following scintillation parameters (illustrated in Fig. 5) were obtained by the simulation for incident x-ray energies of 20 to 60 keV. These are listed next, together with a brief description of their meaning.

1. The absorption fraction $\epsilon$. This parameter is simply the fraction of incident photons absorbed in the scintillator.

2. Energy absorption efficiency $A_e$. This parameter is the fraction of the incident x-ray energy that is absorbed by the scintillator. The quantity is a measure of the light output of the scintillator and is therefore a measure of the scintillator performance. An ideal scintillator will wholly absorb all the x-ray flux at a given energy and would have a value of unity.

3. $K$ escape fraction. The $K$ escape fraction is the ratio of the number of $K$ fluorescence photons that escape from the scintillator to the number of initial interactions.

4. As-absorbed energy distribution moment. This is the moment of the scintillator pulse-height distribution as derived by Swank and was described previously. For a line scintillation spectrum this parameter is unity (i.e., x-ray interactions below the $K$ edge) and will decrease for broad scintillation spectra caused by energy loss (x-ray interactions above the $K$ edge).

## *5.2. Monte-Carlo Simulation Results*

Figure 5 shows the scintillator parameters as a function of incident x-ray energy obtained from the simulation for a scintillator thicknesses of 100 $\mu$m. Below the absorption edge, the energy absorption efficiency of the scintillator follows the photon absorption, since there is no internal energy loss. However, above the absorption edges, this parameter deviates from the absorbed fraction as energy is lost from the scintillator by the escape photons. For this layer thickness, the simulation shows that $\sim$50% of the $K$ shell fluorescent photons escape the scintillator without further interaction and this value remains roughly constant with energy. The greatest deviation and consequently largest value of the energy distribution moment of the broad scin-

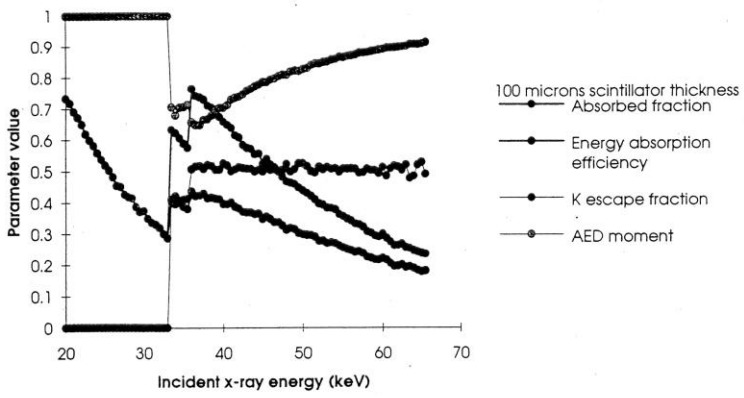


FIGURE 5

TABLE 4

Predicted DQE for X-Ray Energies of 40, 50, and 60 keV

| X-ray energy (keV) | DQE ($\epsilon$) | DQE ($\epsilon$As) |
|---|---|---|
| 40 | 68% | 47% |
| 50 | 45% | 36% |
| 60 | 30% | 26% |

tillation spectrum will occur for an incident x-ray energy just above the $K$ edge. This is because the energy of the fluorescent photon is close to the incident photon energy and so energy loss will have the most pronounced effect on the scintillator efficiency. At higher x-ray energies, the emission line energies represent a decreasing fraction of the total incident x-ray energy. The energy moment of the scintillator spectrum therefore tends toward unity and the absorbed-energy efficiency converges to the values for the absorbed fraction as shown in the simulation.

To illustrate the effect of the $K$ edge on the detector DQE, consider a detector which is quantum limited in its performance (see Section 4) for an incident x-ray energy of 40 keV. The DQE given by Eq. [10] in this region is given by $\epsilon A_s$. Taking values of the parameters from the simulation, the scintillator absorption is around 68% and the parameter $A_s$ has a value of 0.7, giving a DQE of 47%. This value is around 30% lower than the DQE predicted from a simple scintillator absorption model. Table 4 shows tabulated DQE values for incident x-ray energies of 40, 50, and 60 keV along with values calculated by considering just the scintillator absorption alone. As discussed, the most significant loss in DQE occurs for energies just above the $K$ absorption edge up to around 50 keV, emphasizing the need to take into account the effects of the scintillator fluorescence when making predictions about camera system performance.

## 6. CONCLUSION

The effect of the camera PSF and the diffraction spot geometry on the ability of the system to perform low flux dose measurements of Bragg diffraction spots is considered and is shown to limit the performance of the camera compared to simpler models of system performance. This has also emphasized the need for preserving the highest possible spatial resolution of the scintillator. Finally, it has also been shown that the presence of the $K$ edge in a scintillator has a dramatic effect on the DQE for x rays of energy above the absorption edge. In considering, therefore, the performance of the detector in this region, detailed parameters for the scintillator are required to evaluate the DQE. A Monte Carlo simulation of the scintillator would seem to provide a convenient method for evaluating these parameters and therefore predicting the performance of the detector over a wide range of energies.

## ACKNOWLEDGMENTS

The authors are grateful to SERC for research grant support and to SERC Daresbury laboratory for their many helpful comments.

## REFERENCES


1. J. R. HELLIWELL, "Macromolecular Crystallography with Synchrotron Radiation," p. 268, Cambridge Univ. Press, Cambridge, 1992.
2. H. BUTTNER (Ed.), "ESRF Beamline Handbook," Aug. 1993.
3. E. F. EIKENBERRY, M. TATE, D. BILDERBACK, AND S. GRUNER, *in* "Photoelectronic Image Devices 1991" (E. L. Morgan, Ed.), p. 273, IOP, 1992.
4. S. M. GRUNER, S. BARNA, M. WALL, M. TATE, AND E. EIKENBERRY, *Proc. SPIE* **2009,** 98 (1993).
5. C. M. CASTELLI, A. WELLS, K. MCCARTHY, AND A. HOLLAND, *Nucl. Instrum. Methods. A* **310,** 240 (1991).
6. P. BAILEY, C. CASTELLI, M. CROSS, P. ESSEN, A. HOLLAND, F. JANSEN, P. DE KORTE, P. POOL, AND P. VERHOEVE, *Proc. SPIE* **1344** (1990).
7. G. BERTOLINI AND A. COCHE, "Semiconductor Detectors," Elseveir–North-Holland, Amsterdam, 1968.
8. N. M. ALLINSON, P. CARR, M. COLAPIETRO, M. HARDING, J. HELLIWELL, A. THOMPSON, AND S. WEISGERBER, *Phase Transitions* **39,** 145 (1992).
9. C. COLEMAN, *Adv. Electron. Electron Phys.* **64B,** 649 (1985).
10. S. KUBOTA, H. MURAKAMI, J. RUAN, AND N. IWASA, *Nucl. Instrum. Methods A* **310,** 645 (1991).
11. J. DREWERY, G. CHO, I. FUJIEDA, T. JING, S. KAPLAN, V. PEREZ-MENDEZ, AND D. WILDERMUTH, *Nucl. Instrum. Methods A* **310,** 165 (1991).
12. G. KNOLL, "Radiation Detection and Measurement," p. 244, Wiley, New York, 1989.
13. A. STEVELS AND A. SCHRAMA-DE PAUW, *Philips Res. Rep.* **29,** 340 (1974).
14. K. OBA, M. ITO, AND M. YAMAGUCHI, *Adv. Electron. Electron Phys.* **74,** 247 (1988).
15. C. M. CASTELLI, N. ALLINSON, AND K. MOON, *Nucl. Instrum. Methods A* **348,** 649 (1994).
16. S. GRUNER, J. MILCH, AND G. REYNOLDS, *IEEE Trans. Nucl. Sci.* **25,** No. 1, 562 (1978).
17. K. KALATA, M. STANTON, AND W. PHILIPS, *J. X-ray Sci. Technol.* **3,** 157 (1992).
18. I. FUJIEDA, G. CHO, J. DREWERY, T. GEE, T. JING, S. KAPLAN, V. PEREZ-MENDEZ, AND D. WILDERMUTH, *IEEE Trans. Nucl. Sci.* **38,** No. 2, 255 (1991).
19. R. K. SWANK, *J. Appl. Phys.* **44,** No. 9, 4199 (1973).
20. N. A. DYSON, "X-Rays in Atomic and Nuclear Physics," Appendix 4, Cambridge Univ. Press, Cambridge, 1990.
21. "International Tables for X-Ray Crystallography," Vol IV, Kynoch Press, Birmingham, 1974.
22. J. H. HUBBELL, Photon Mass Attenuation Coefficients, *Int. J. Appl. Radiation Isotopes* **33,** (1982).